PREPRINT
under review

Modelling void fraction distributions in breaking hydraulic jumps

Hong Hu[1], Hang Wang[1], Matthias Kramer[2*]

[1] State Key Laboratory of Hydraulics and Mountain River Engineering, Sichuan University, Chengdu 610065, China
[2] School of Engineering and Technology (SET), The University of New South Wales, Canberra, ACT 2610, Australia

ABSTRACT
We present two models for predicting void-fraction distributions in hydraulic jumps, addressing the limitations of the conventional two-layer formulation in representing continuous profiles. The first model introduces a two-state convolution to describe the smooth transition between the turbulent shear and roller regions, while the second applies a superposition framework to capture the overlapping contributions from both layers. Validation against experimental data shows that both models improve the representation of the transition region and provide a more realistic connection between the upper and lower aerated layers. The proposed formulations not only reproduce measured profiles more accurately but also provide a continuous and physically consistent description across the entire flow depth. These models offer a practical tool for hydraulic design and advance the understanding of vertical mass transport in highly aerated flows.

KEYWORDS
Hydraulic jump; void fraction; two-layer model; two-state convolution model; superposition model

1. Introduction

A hydraulic jump is a rapid transition in open-channel flow in which the water surface rises abruptly due to a sudden deceleration of the supercritical flow. This transition typically produces intense turbulent mixing between the high-velocity impinging jet and the slower receiving water, as well as between the breaking water and the surrounding air. The resulting air–water mixture forms a highly complex two-phase flow characterized by bubbles of varying size, shape, and velocity, continuously distorted by vortices, shear, and pressure fluctuations (Valero et al., 2024). Understanding this interaction is essential for hydraulic design, and considerable research has therefore focused on the mechanisms of air entrainment, two-phase turbulence, and the resulting void fraction distribution (Chanson & Brattberg, 2000; Kramer & Valero, 2020; Wang & Chanson, 2015; Wang, Murzyn, & Chanson, 2014).

Reliable measurements of void fractions within highly turbulent and aerated flows have been achieved since the 1950s using conductivity phase-detection probes (Rajaratnam, 1962;

* Corresponding author's email: m.kramer@unsw.edu.au

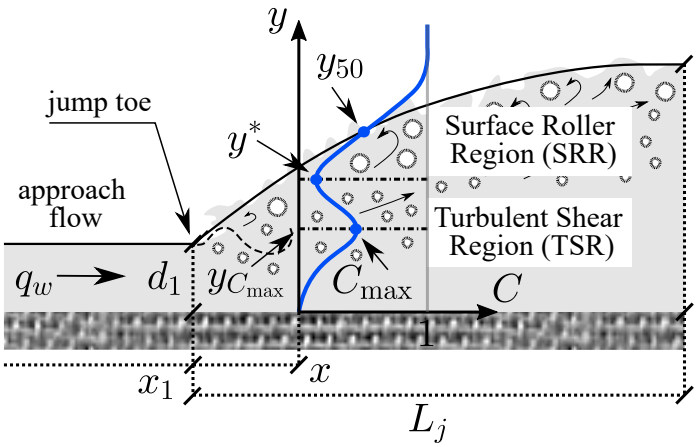

Figure 1. Sketch of typical void fraction distribution at a vertical cross-section in hydraulic jump; q_w = specific water flow rate; d_1 = inflow depth; x_1 = jump toe location; x = streamwise profile location; C = void fraction; $C_{\max}$ = maximum void fraction below mean interface position y^*; $y_{C_{\max}}$ = elevation where $C = C_{\max}$; y_{50} = elevation where $C = 0.5$; y = vertical coordinate; L_j = jump length.

Straub & Anderson, 1958). These probes intrusively record the residence time of the sensor tip within the water and air phases of the two-phase flow, based on the distinct electrical resistivities of water and air (Chanson, 2002; Crowe, Sommerfeld, & Tsuji, 2011). The time-averaged volumetric void fraction, C, at a given measurement point is then calculated from the probe signal as

$$C = \frac{\mathcal{V}_a}{\mathcal{V}_a + \mathcal{V}_w} = \frac{t_a}{t_a + t_w}, \tag{1}$$

where $\mathcal{V}$ denotes the volume, and t represents the time during which the probe tip is immersed in either phase over the sampling duration; the subscripts a and w stand for air and water, respectively.

Figure 1 presents a schematic of a typical void fraction profile across a vertical cross-section of a classical hydraulic jump. The characteristic "double-S" shape reflects the underlying flow structure, which can be divided into two primary regions: a Turbulent Shear Region (TSR) near the channel bed and a Surface Roller Region (SRR) above it (Long, Rajaratnam, Steffler, & Smy, 1991). These regions merge approximately at the location of the local minimum void fraction, denoted by y^*.

In the TSR ($y < y^*$), air is entrained at the jump toe in the form of air pockets, generated by the combined action of the impinging jet and the reversing roller toe. These air pockets are rapidly broken into smaller bubbles by turbulent shear and are subsequently transported downstream while being diffused and detrained. The void fraction distribution in this region follows the theoretical solution of an advective–diffusion equation for air bubbles in water, resulting in a Gaussian profile. In the SRR ($y > y^*$), air entrainment occurs at the roller free surface in a manner analogous to broken standing waves or plunging waves. The characteristics of this entrainment depend on the Froude and Reynolds numbers, which quantify the jump's flow strength and turbulence. The air–water mixture in this free-surface layer consists of a dispersed bubbly flow, as well as a wavy free surface that traps and transports air between surface waves, ripples, and other roughness elements. Consequently, the void fraction in the SRR results from the combined contribution of these processes, increasing from the local minimum at $y = y^*$ to unity at the free surface.

Traditionally, the void fraction distribution across the full depth of a hydraulic jump is described using two separate formulations, one for each region (Wang, 2014), which intersect approximately at y^*. This approach is herein referred to as the conventional two-layer void fraction model. The model has been successfully applied in numerous studies and has demonstrated robust agreement with experimental measurements (Murzyn, Mouaze, & Chaplin, 2005; Wang & Chanson, 2016).

However, by dividing the hydraulic jump flow into two layers with distinct flow mechanisms, the conventional two-layer model neglects the continuous nature of the air content distribution, particularly the air exchange between the TSR and SRR. This limitation is especially pronounced near the jump toe, where the two layers partially overlap. In this work, we propose extensions to the two-layer model that improve the fit to measured void fraction data in the transition region and provide a unified view of the underlying aeration processes. The first extended model is formulated as a convolution of the conventional two-layer formulations, inspired by recent studies on self-aerated sloping chute flows (Kramer, 2024; Kramer & Valero, 2023), and is referred to as the **two-state convolution model**. The second extended model employs a simpler approach, consisting of a linear addition of the two-layer formulations, and is referred to as the **superposition model**. Both models are evaluated against experimental data from hydraulic jumps at three different Froude numbers.

Overall, these extensions provide a unified representation of the void fraction distribution in hydraulic jumps, resolve partially masked peaks, and offer new insights into the streamwise evolution of aeration mechanisms by linking the TSR and SRR within a continuous representation of their combined contributions.

2. Methods

2.1. Conventional two-layer model

The two-layer structure of a hydraulic jump forms the basis of the conventional two-layer model, which characterizes the variation of void fraction across the jump depth (Wang, 2014).

Chanson (1995) derived an analytical solution for the void fraction distribution in the TSR by analogy with a vertical supported jet. Neglecting compressibility effects, the vertical transport of bubbles in a two-dimensional steady flow is governed by the advection–diffusion equation for air in water

$$V_1 \frac{\partial C}{\partial x} + u_r \frac{\partial C}{\partial y} = D_t \frac{\partial^2 C}{\partial y^2}, \tag{2}$$

where C is the time-averaged void fraction, x is the streamwise coordinate, y is the vertical coordinate measured from the channel bed, V_1 is the horizontal advection velocity, assumed equal to the approach flow velocity, u_r is the bubble rise velocity, and D_t is the vertical diffusion coefficient.

To solve Eq. (2), it is assumed that u_r and D_t are constant. Introducing the transformed longitudinal coordinate $X = x - x_1 + (u_r/V_1)y$, where x_1 denotes the jump toe location, Eq. (2) can be rewritten in the form of a classical two-dimensional diffusion equation (Crank, 1956)

$$V_1 \frac{\partial C}{\partial X} = D_t \frac{\partial^2 C}{\partial y^2}. \tag{3}$$

Approximating air entrainment at the jump toe as a point source, the characteristic solution

of Eq. (3) is (Cummings & Chanson, 1997)

$$C_{\mathrm{TSR}} = \frac{Q_a/Q_w}{\sqrt{4\pi D^{\#} X'}} \left(\exp\left(-\frac{(Y'-1)^2}{4D^{\#}X'} \right) - \exp\left(-\frac{(Y'+1)^2}{4D^{\#}X'} \right) \right), \tag{4}$$

where Q_a and Q_w are the air and water flow rates at the jump toe, $X' = X/d_1$, $Y' = y/d_1$, and $D^{\#} = D_t/(V_1 d_1)$ is the dimensionless diffusivity in the TSR, with d_1 the inflow depth at $x = x_1$ (Fig. 1). The second term on the right-hand side of Eq. (4) represents a mirror source introduced to satisfy the zero-void-fraction condition at the bed ($Y' = 0$). Since its effect is appreciable only in the immediate vicinity of the bed, this term is commonly omitted. For practical data fitting, the prefactor in Eq. (4) is replaced by the experimentally measurable maximum void fraction C_{max}, giving a Gaussian approximation

$$C_{\mathrm{TSR}} = C_{\mathrm{max}} \exp(-\Psi_1^2), \quad \text{if } y < y^* \tag{5}$$

with

$$\Psi_1 = \frac{\left(y - y_{C_{\mathrm{max}}}\right)}{2\sqrt{D^{\#}\,(x - x_1)\,d_1}}, \tag{6}$$

where y^* marks the transition between the TSR and SRR.

Above y^*, the flow enters the SRR, where the void fraction distribution can be described using a Gaussian error function by analogy with interfacial aeration in a uniform-velocity water jet (Brattberg, Chanson, & Toombes, 1998; Chanson, 1995; Murzyn et al., 2005; Wang, 2014)

$$C_{\mathrm{SRR}} = \frac{1}{2}\left(1 + \mathrm{erf}\left(\Psi_2\right)\right) \quad \text{if } y > y^*, \tag{7}$$

with

$$\Psi_2 = \frac{(y - y_{50})}{2\sqrt{D^{*}\,(x - x_1)\,d_1}}, \tag{8}$$

where y_{50} is the characteristic elevation at which $C = 0.5$ (Fig. 1), and $D^* = D_t/(V_1 d_1)$ is a dimensionless diffusivity in the SRR. This diffusivity reflects the combined effect of entrained bubbles and air intermittently trapped by the free-surface turbulence.

An alternative interpretation of the SRR void fraction considers that the air content is not governed by an advection–diffusion process, but rather arises from the wavy nature of the free surface. In this view, the surface elevation distribution can be approximated as Gaussian, and the resulting air concentration corresponds to its cumulative distribution. Mathematically, this can be expressed using a Gaussian error function (Valero & Bung, 2016), which is formally equivalent to Eq. (7). This perspective emphasizes that the observed void fraction arises from the combined effects of air entrapped within surface waves and entrained bubbles (Kramer & Valero, 2023). For consistency with the rest of the analysis, we retain Eq. (7); however, this alternative interpretation provides additional insight into the turbulent diffusivity D^*. In particular, the denominator in Eq. (8), $\sqrt{D^*(x - x_1)d_1}$, can be interpreted as the effective thickness of the aerated layer near the free surface (Kramer, 2024; Kramer & Valero, 2023), thereby connecting the diffusion-based model directly to the wave-driven air distribution.

2.2. Two-state convolution model

The conventional two-layer model performs well in describing experimental void fraction data; however, it neglects interface-driven vertical transport by dividing the hydraulic jump into two separate regions. To address this limitation, the two-state convolution model extends the classical two-layer framework by maintaining the independence of both layers while coupling them through the concept of a fluctuating interface. This concept for vertical air transport was first proposed by Kramer and Valero (2023) for smooth and stepped spillway flows. Here, we adapt this approach to hydraulic jumps to describe the dynamic connection between the TSR and SRR. This adaptation yields the following expression for the void fraction distribution

$$C = \underbrace{C_{\max} \exp(-{\Psi_1}^2)}_{=C_{\mathrm{TSR}}} \; (1 - \Gamma) + \underbrace{\frac{1}{2} \left(1 + \operatorname{erf}\left(\Psi_2\right)\right)}_{=C_{\mathrm{SRR}}} \; \Gamma, \tag{9}$$

where the weight function Γ results from a convolution of a Gaussian interface probability with a quasi-instantaneous void fraction distribution

$$\Gamma = \frac{1}{2} \left(1 + \operatorname{erf}\left(\frac{y - y^*}{\sqrt{2}\sigma^*}\right)\right), \tag{10}$$

with σ^* representing the standard deviation of the interface distribution. Here, y^* represents the mean interface position and has the same meaning as in the conventional two-layer model. The mathematical derivation for this framework is presented in Kramer and Valero (2023); Krug, Philip, and Marusic (2017). In comparison with the the conventional two-layer model, one additional parameter, σ^*, is introduced, which characterizes the standard deviation of the interface fluctuations; this addition allows a more accurate representation of the interaction between the TSR and SRR and produces a continuous void fraction profile.

It is noteworthy that the two-state convolution model treats the TSR and SRR independently, assuming that each layer is governed by a distinct physical process: air entrainment by the impinging jet at the jump toe and subsequent turbulent bubble breakup in the TSR, and free-surface fluctuations, associated with entrainment and large air voids, in the SRR. In this way, it constitutes a direct extension of the conventional two-layer model.

2.3. Superposition model

Another, mathematically simpler approach is the superposition model, which is derived directly from mass conservation considerations and assumes a linear superposition of different air fractions. Unlike the two-state convolution model, which explicitly accounts for the coupling between the TSR and SRR through the concept of a fluctuating interface, the superposition model treats the contributions of the two layers as additive, without explicitly modeling the dynamic interaction between them. This approach was previously employed by R. Bai, Tang, Murzyn, and Wang (2023) and Kramer (2024). Here, we extend its application to hydraulic jump flows, considering both the TSR and SRR, and represent the total void fraction as

$$C = \underbrace{C_{\max} \exp(-{\Psi_1}^2)}_{=C_{\mathrm{TSR}}} + \underbrace{\frac{1}{2} \left(1 + \operatorname{erf}\left(\Psi_2\right)\right)}_{=C_{\mathrm{SRR}}}. \tag{11}$$

Unlike the conventional two-layer model and the two-state formulation, the superposition

model does not require the specification of the parameter y^*; this is a direct consequence of assuming that the physical processes in the TSR and SRR are preserved throughout the entire depth of the flow.

By treating the contributions as linearly additive, the superposition model accounts for both the TSR and SRR but does not consider the coupling between these layers, unlike the two-state convolution approach. Despite this limitation, it remains useful for practical applications where a straightforward yet reasonably accurate description of the void fraction is required.

2.4. Determination of model parameters

The model parameters for the three approaches were determined using a fitting procedure implemented in MATLAB, applied to our experimental dataset of void fraction profiles. Table 1 lists the fixed and free parameters for the models. All free parameters were estimated simultaneously using a nonlinear least-squares optimisation procedure, in which the complete parameter vector was updated iteratively at each optimisation step, subject to physically motivated bounds. In cases where a two-step fitting strategy was employed, this simultaneous optimisation was applied independently at each fitting step. The fitting procedure for each model is described below.

- **Conventional two-layer model:** The characteristic depth y_{50} and the transition depth y^* were first determined from each profile, characterized by the position relative to the jump toe, $(x - x_1)$, and the inflow depth, d_1. Previous literature effectively treats the maximum void fraction, $C_{\max}$, of the TSR ($y < y^*$) and its corresponding bed-normal elevation, $y_{C_{\max}}$, as directly measurable; however, due to data scatter, these quantities are typically fitted and treated as free parameters. Accordingly, the TSR profile, Eq. (5), was fitted to the data for $y < y^*$ by adjusting $C_{\max}$, $y_{C_{\max}}$, and $D^{\#}$, while Eq. (7) was fitted for $y > y^*$ by adjusting D^*.
- **Two-state convolution model:** The parameters y_{50}, y^*, $(x-x_1)$, and d_1 were taken from the measurements, and a two-step fitting procedure was adopted. First, the SRR profile was fitted using Eq. (7) for $y > y^*$. In the second step, the two-state profile, Eq. (9), was fitted to the full void fraction profile. The parameters y_{50} and D^* were kept fixed from the first step, while $C_{\max}$, $y_{C_{\max}}$, $D^{\#}$, and σ^* were adjusted to minimize deviation. y^* was allowed to vary slightly to improve the overall fit.
- **Superposition model:** Parameters y_{50}, x, x_1, and d_1 were treated as fixed, while $C_{\max}$, $y_{C_{\max}}$, $D^{\#}$, and D^* were optimized in a single step by fitting Eq. (11).

Table 1. Fixed and free model parameters for the three approaches.

Approach	Fixed parameters	Free parameters
Conventional two-layer model	y_{50}, y^*, x, x_1, d_1	$C_{\max}$, $y_{C_{\max}}$, $D^{\#}$, D^*
Two-state convolution model	y_{50}, y^*, x, x_1, d_1	$C_{\max}$, $y_{C_{\max}}$, $D^{\#}$, D^*, σ^*
Superposition model	y_{50}, x, x_1, d_1	$C_{\max}$, $y_{C_{\max}}$, $D^{\#}$, D^*

Treating $C_{\max}$ and $y_{C_{\max}}$ as free parameters reflects a deliberate modelling decision and was particularly necessary for the superposition model to achieve meaningful void fraction profiles; without this adjustment, the model would fail to represent the measurements accurately. For the two-state convolution model, allowing $C_{\max}$ and $y_{C_{\max}}$ to vary also improves the fit, although the model can still provide reasonable profiles even if partially constrained.

In particular, for the two-state convolution model, apparent peaks may arise from the interaction and overlap between the TSR and the SRR, whereby the "true" underlying peak is partially masked. In the superposition model, the observed peak is an emergent feature of the combined contributions and may not correspond to a maximum of any single component. By treating $C_{\max}$ and $y_{C_{\max}}$ as free parameters, both models can capture these emergent or composite peak behaviours while allowing the assumed functional forms to be applied consistently.

Consequently, while both models offer practical and reasonably accurate descriptions of the void fraction distribution, the interpretation of $C_{\max}$ and $y_{C_{\max}}$ is less direct than in models where these quantities are directly measured, yet remains physically meaningful. This aspect is discussed further in Section 4.1.

2.5. Experimental facilities and flow conditions

Experiments were conducted in a horizontal rectangular flume measuring 9.95 m in length, 0.4 m in width, and 0.5 m in depth, with glass bottom and sidewalls. Water was supplied from a large head tank with a bottom area of 2.5 m times 3 m and a height of 5 m, equipped with a gradually converging bottom outlet with rectangular cross-section. The outlet measures 0.4 m in width and 0.03 m in height at the junction with the flume, where the longitudinal distance $x = 0$. An overshoot tailgate at the downstream end of the flume was used to control the tailwater level and position the hydraulic jump toe at $x_1 = 4$ m. The outflow was measured using a full-width sharp-crested weir before being recirculated to an underground reservoir.

Table 2. Experimental flow conditions and recorded profiles.

q_w (m^2/s)	d_1 (m)	V_1 (m/s)	Fr_1 (-)	Re (-)	L_j (m)	$(x - x_1)$ (m)
0.132	0.0410	3.21	5.1	1.32×10^5	0.91	0.15, 0.3, 0.45, and 0.65
0.154	0.0411	3.74	5.9	1.54×10^5	1.16	0.15, 0.3, 0.45, 0.65, and 0.85
0.182	0.0380	4.80	7.9	1.82×10^5	1.61	0.15, 0.3, 0.45, 0.65, 0.85, and 1.1

We used a conductivity phase-detection probe, manufactured at Sichuan University, to measure the void fraction, as employed in R. Bai et al. (2023); Wang, Bai, Bai, and Liu (2022), among other studies. The probe consists of a platinum inner electrode with a diameter of 0.1 mm and a stainless-steel outer electrode with a diameter of 0.8 mm, with a longitudinal tip separation of 10.0 mm and a spanwise separation of 2.0 mm. This needle sensor was aligned with the main flow direction during the experiments, recording air–water phase changes at the sensor tip. The sampling frequency and duration at each measurement point were 40 kHz and 60 s, respectively, in line with comparable studies, see Chanson and Brattberg (2000, 20 kHz, 10 s), Wang (2014, 20 kHz, 45 s), Wang and Chanson (2018, 20 kHz, 45 s), Kramer and Valero (2020, 20 kHz, 90 s), Z. Bai, Bai, Tang, Wang, and Liu (2021, 20 kHz, 45 s), and R. Bai et al. (2023, 20 kHz, 45 s).

Three hydraulic jumps were tested with inflow Froude numbers $Fr_1 = 5.1$, 5.9 and 7.9. Here, $Fr_1 = V_1/\sqrt{gd_1}$ is defined using the inflow depth d_1 and the mean velocity $V_1 = q_w/d_1$, where q_w is the specific flow rate and g is the gravitational acceleration. The corresponding Reynolds numbers, defined as $Re = q_w/\nu$, ranged from 1.32×10^5 to 1.82×10^5, where ν is the kinematic viscosity. Air-water flow properties were recorded at up to six cross-sections as per Table 2 at the centreline.

3. Results

3.1. Void fraction distributions and their modelling

The time-averaged void fraction distributions measured with the phase-detection probe are presented in Fig. 2 for three cross-sections of the tested hydraulic jumps. At each cross-section, the experimental data are compared with the analytical profiles obtained from the conventional two-layer model, the two-state convolution model, and the superposition model, respectively.

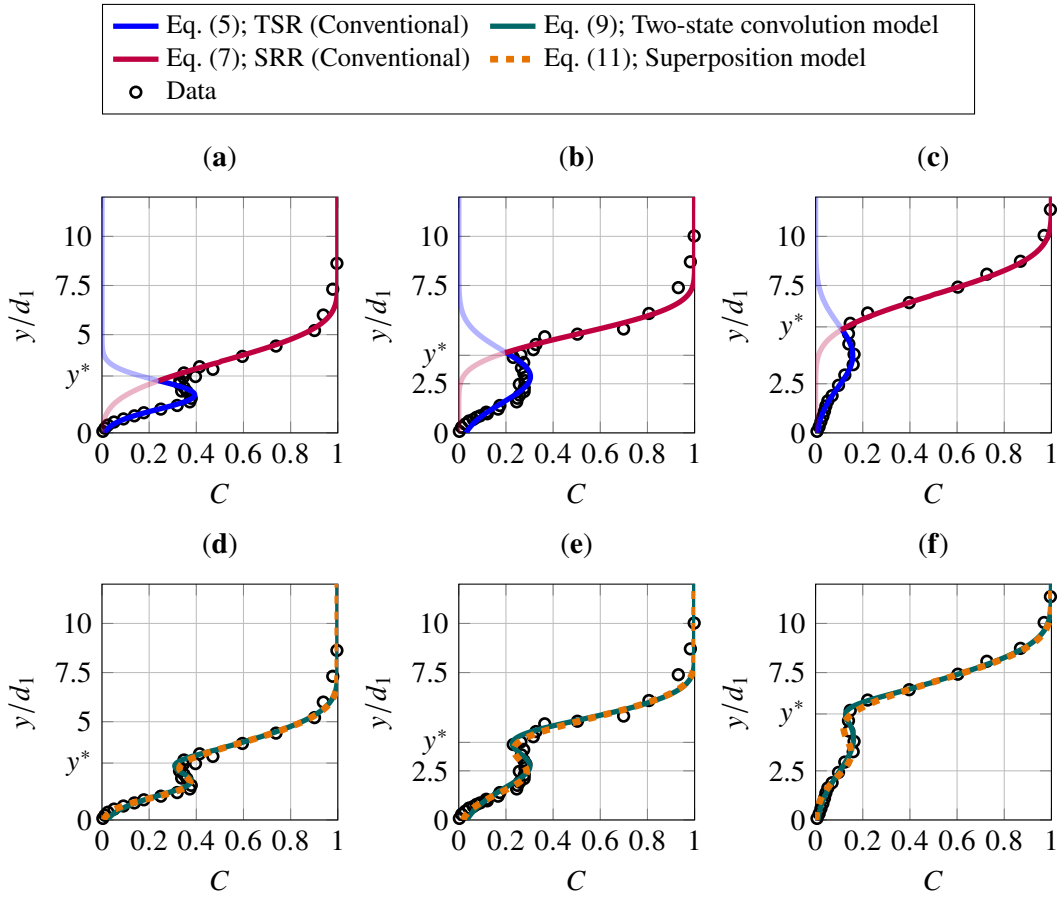

Figure 2. Application of the three modelling approaches to measured void fraction distributions along the hydraulic jump centerline with $Fr_1 = 7.9$: (**a**, **d**) $(x - x_1)/L_j = 0.19$; (**b**, **e**) $(x - x_1)/L_j = 0.28$; (**c**, **f**) $(x - x_1)/L_j = 0.53$. Equations (5) and (7) are also used in the two-state convolution and superposition models, but are not plotted in panels (**d**) - (**f**) to maintain readability.

It is observed that the conventional two-layer model reproduces the measured void fraction profiles with good accuracy across the two characteristic layers of the flow (Figs. 2**a**,**b**,**c**). Specifically, the model captures the Gaussian-shaped void fraction within the TSR and the gradual decay of void fraction in the SRR, which follows an error function. The model accurately describes the void fraction both near the jump toe and towards the downstream end of the jump, indicating that its underlying assumptions are well suited to representing the overall structure of the hydraulic jump. However, the transition between TSR and SRR is not accurately captured, due to the idealized assumption of a sharp interface between the layers.

Both the two-state convolution model and the superposition model provide a continuous

representation of the void fraction across the entire flow depth (Figs. 2**d**–**f**) by explicitly accounting for the coexistence of the TSR and SRR within a single vertical profile. The two-state convolution model achieves this by convolving the Gaussian distribution of the TSR with the error-function representation of the SRR, whereas the superposition model expresses the void fraction as the additive combination of the two characteristic distributions. This unified description enables both models to provide a more physically consistent representation of the internal structure of the hydraulic jump than the classical two-layer approach. For completeness, all measured void-fraction profiles, together with the corresponding fits obtained using both the two-state convolution and superposition models, are provided in Appendix A.

Figure 3 shows the root mean squared error between the model predictions and the experimental measurements across the investigated flow conditions. Here, profiles 1 to 4 correspond to $Fr_1 = 5.1$, profiles 5 to 9 to $Fr_1 = 5.9$, and profiles 10 to 15 to $Fr_1 = 7.9$. Within each group, the profile number increases with streamwise distance from the jump toe (see Table 2), and all profiles are shown in Appendix A. The root mean squared error remains below $5 \cdot 10^{-2}$ for all three models, indicating consistently good agreement with the measurements. Overall, the two-state convolution and superposition models exhibit slightly lower errors than the two-layer model, particularly for datasets with the highest Fr_1, which appears to result from the two-layer model missing the transition between TSR and SRR. This suggests that the two-state convolution and superposition approaches more accurately capture the flow structure across the full range of flow conditions.

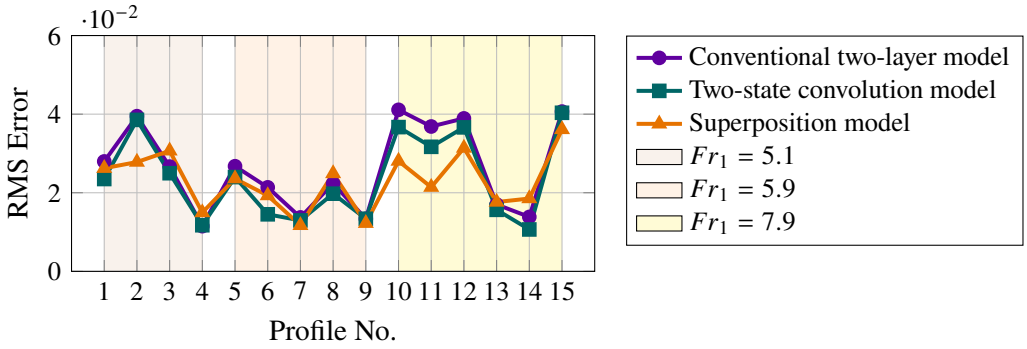

Figure 3. RMS error comparison across the three models. RMS values were computed as the root mean square of the differences between the measured void fraction and the fitted profile at all vertical measurement points for each model: conventional two-layer model [Eqns. (5) and (7)], two-state convolution model [Eq. (9)], and superposition model [Eq. (11)].

3.2. Model parameters

Figure 4 shows the model parameters for the three approaches. The streamwise distance $(x - x_1)$ and the inflow depth d_1 are derived from the respective experimental conditions for each profile and are implicitly represented along the abscissa, as $L_j = f(Fr_1, d_1)$. The other model parameters, including $C_{\max}$, $y_{C\max}$, $D^{\#}$, y^*, y_{50}, and D^*, characterize key features of the aerated flow, such as the maximum void fraction, its corresponding elevation, the diffusivities of the TSR and SRR, and characteristic flow depths, allowing a direct comparison of how each model captures the flow structure across the studied conditions.

For the TSR, the two-state convolution and superposition models tend to predict slightly higher or lower $C_{\max}$ values and elevations $y_{C\max}$ than the two-layer model (Fig. 4**a**,**b**), which are discussed further in Section 4.1. These differences are most pronounced near the jump toe, where the interaction between the impinging jet and the surface roller strongly

influences the void fraction distribution. Moving downstream, the discrepancies between the models decrease, and the predicted profile shapes converge, indicating that all three approaches effectively capture the bulk flow structure at larger distances from the jump. These differences in the TSR are also reflected in the associated dimensionless diffusivities $D^{\#}$ (Fig. 4**c**), which vary slightly among the models and highlight the differences in how each approach represents the spreading of the Gaussian void fraction profile.

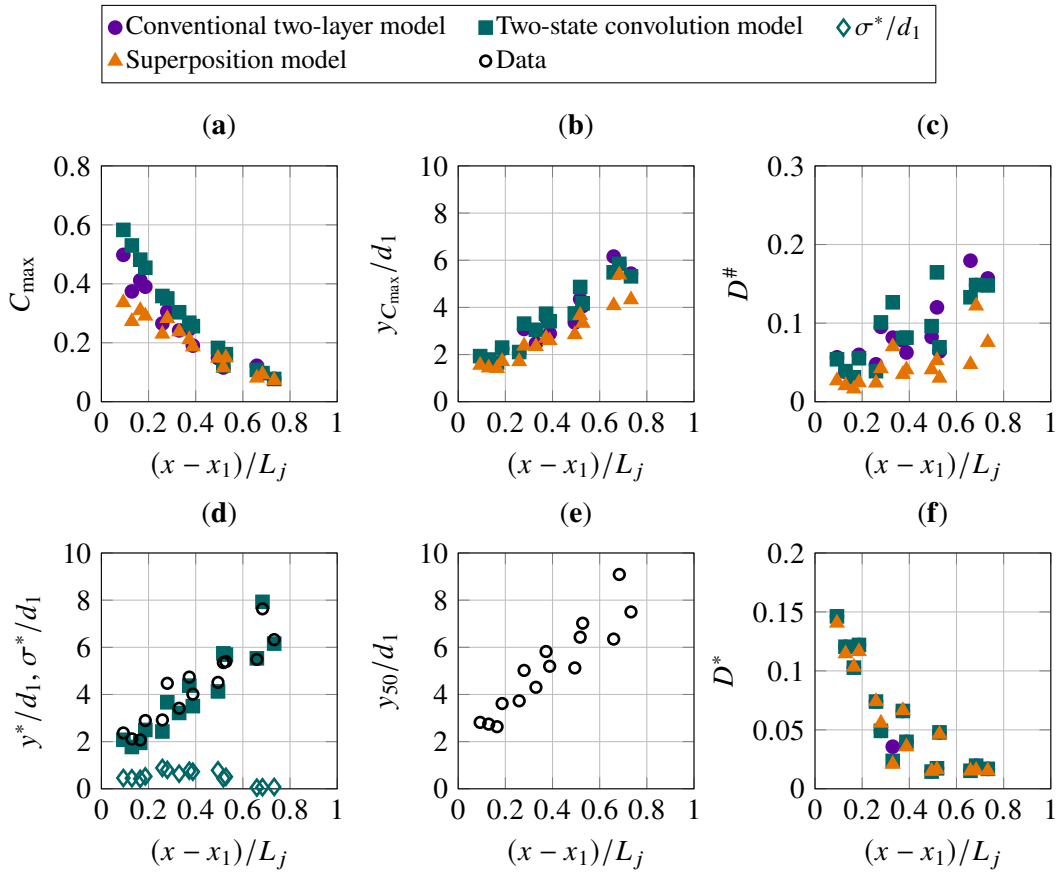

Figure 4. Comparison of model parameters for the three modeling approaches: (**a**) Maximum void fraction C_{max} of the TSR; (**b**) Corresponding location y_{Cmax}; (**c**) Dimensionless diffusivity $D^{\#}$ of the TSR; (**d**) Interface parameters y^* and σ^*; (**e**) Mixture flow depth y_{50} of the SRR; (**f**) Dimensionless diffusivity D^* of the SRR.

The transition parameter, or mean interface position, y^*, separates the TSR from the SRR in a time-averaged sense. Figure 4**d** shows the streamwise evolution of y^* for the two-layer and the two-state convolution models, demonstrating only subtle differences between the approaches, as well as a nearly linear increase of y^* with streamwise distance from the jump toe. This trend reflects the gradual thickening of the TSR and the progressive separation between the upper and lower aerated regions. For completeness, the corresponding standard deviation, σ^*/d_1, ranged between 0.05 and 0.8 (Fig. 4**d**, diamonds), indicating moderate variability along the jump. The largest fluctuations occurred near the impingement region, where turbulence and jet–roller interactions are strongest, and decreased downstream as the flow developed and the interface became more stable.

Having described the behaviour of the TSR and the transition, we turn our attention to the parameters of the SRR. The characteristic mixture depth, y_{50} was directly extracted from the

experimental data and is therefore not model-specific. As shown in Fig. 4**e**, y_{50} exhibits a nearly linear increase with streamwise distance from the jump toe, reflecting the gradual growth of the mixture depth along the hydraulic jump. The associated diffusivity, D^*, shown in Fig. 4**f**, characterizes the thickness of the SRR for the three models. Practically, the estimation of D^* was not significantly affected by the selection of the void fraction model, as reflected by the very similar data distributions. Furthermore, D^* was observed to decrease exponentially with streamwise distance, which is consistent with previous observations reported in the literature.

Overall, the combined analysis of TSR parameters ($C_{\max}$, $y_{C\max}$, and $D^{\#}$), the transition parameters (y^* and σ^*), and SRR characteristics (y_{50} and D^*) demonstrates how the different modeling approaches capture the structure of the aerated flow. The two-state convolution and superposition models provide a smoother and more continuous representation of the flow, particularly near the jump toe where interactions between the impinging jet and the surface roller are strongest. Downstream, all models converge toward similar predictions, indicating that the bulk flow structure is well captured across approaches. Notably, empirical correlations and fits for these parameters have been provided in previous studies (Wang, 2014; Wang & Chanson, 2018), which offer a useful reference for comparison and validation of model predictions under varying flow conditions.

3.3. Streamwise evolution of depth-averaged void fraction

The mean void fraction is a key parameter in hydraulic design and arises from a depth-averaging process of the void fraction profile. It is here evaluated using the three presented modelling approaches. In the conventional approach, the mean concentration is computed as a sum of the depth-averaged contributions from each layer

$$\langle C\rangle_{\text{Conventional}} = \underbrace{\frac{1}{y_{90}}\int_{y=0}^{y^*} C_{\text{TSR}}\,\mathrm{d}y}_{=\langle C\rangle_{\text{TSR}}} + \underbrace{\frac{1}{y_{90}}\int_{y=y^*}^{y_{90}} C_{\text{SRR}}\,\mathrm{d}y}_{=\langle C\rangle_{\text{SRR}}}, \tag{12}$$

where $\langle C\rangle_{\text{TSR}}$ and $\langle C\rangle_{\text{SRR}}$ are the contributions from the TSR and the SRR, respectively, and y_{90} is the mixture flow depth, defined as the height where $C = 0.9$. The two-state model, in contrast, accounts for the intermittent occurrence of TSR and SRR structures across the flow depth by introducing a local occurrence probability, Γ. The contributions from each region are weighted by $(1-\Gamma)$ and Γ, respectively, giving

$$\langle C\rangle_{\text{Two-state}} = \underbrace{\frac{1}{y_{90}}\int_{y=0}^{y_{90}} C_{\text{TSR}}\,(1-\Gamma)\,\mathrm{d}y}_{=\langle C\rangle_{\text{TSR}}} + \underbrace{\frac{1}{y_{90}}\int_{y=0}^{y_{90}} C_{\text{SRR}}\,\Gamma\,\mathrm{d}y}_{=\langle C\rangle_{\text{SRR}}}. \tag{13}$$

Finally, the superposition approach treats the two regions as fully overlapping over the entire depth, so that the mean concentration is the simple sum of the depth-averaged concentrations of TSR and SRR

$$\langle C\rangle_{\text{Superposition}} = \underbrace{\frac{1}{y_{90}}\int_{y=0}^{y_{90}} C_{\text{TSR}}\,\mathrm{d}y}_{=\langle C\rangle_{\text{TSR}}} + \underbrace{\frac{1}{y_{90}}\int_{y=0}^{y_{90}} C_{\text{SRR}}\,\mathrm{d}y}_{=\langle C\rangle_{\text{SRR}}} \tag{14}$$

The overall trend in Figures 5**a**,**b**,**c** shows the decomposition of the mean void fraction

$\langle C \rangle$ into $\langle C \rangle_{\mathrm{TSR}}$ and $\langle C \rangle_{\mathrm{SRR}}$. The mean void fraction decreases with increasing streamwise distance, which is also reflected in reductions of both $\langle C \rangle_{\mathrm{TSR}}$ and $\langle C \rangle_{\mathrm{SRR}}$. Within the SRR, the void fraction remains consistently higher than in the TSR (Figs. 5**b**,**c**), reflecting the presence of large voids and pockets of entrapped air rather than fine, entrained bubbles. This pattern is consistent with the jump toe acting as a primary source of both air entrainment and turbulence generation, which gives rise to pronounced surface fluctuations. These fluctuations and the associated entrainment processes progressively weaken downstream, resulting in a gradual decay of the overall void fraction.

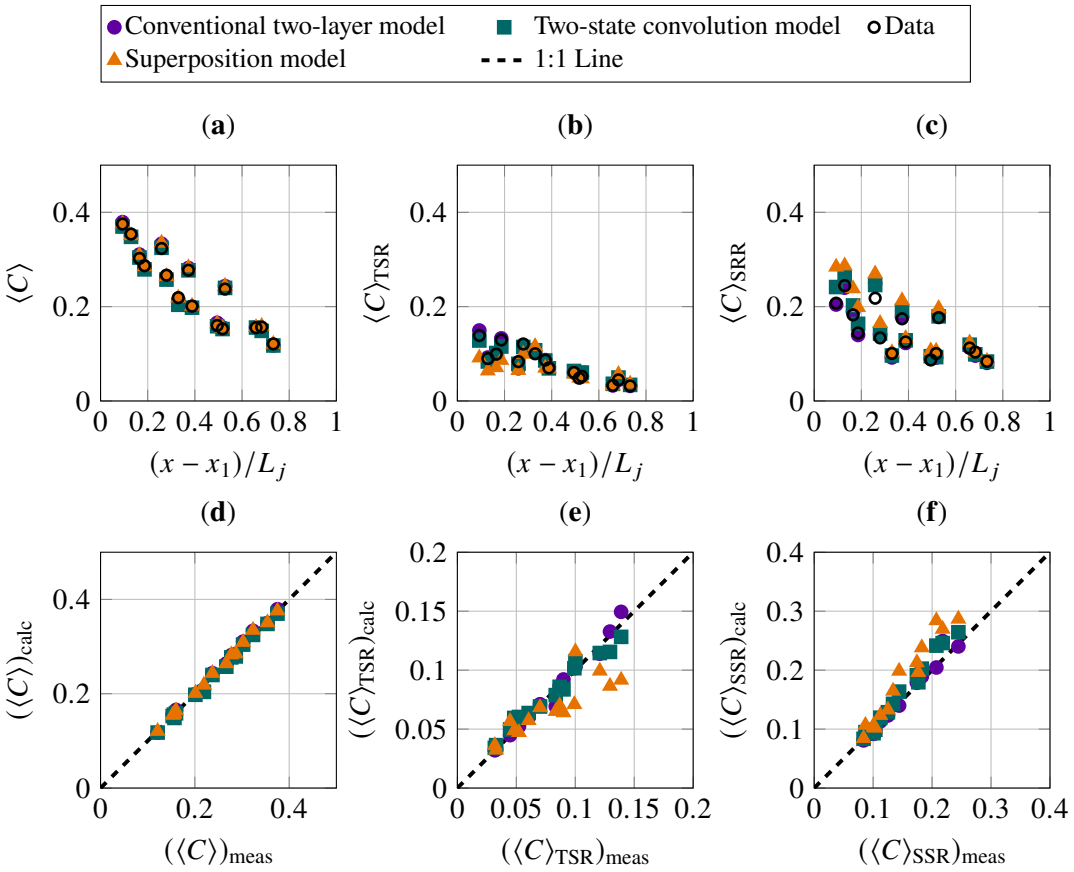

Figure 5. Streamwise decomposition of the depth-averaged (mean) void fraction: (**a**, **d**) Total void fraction; (**b**, **e**) Void fraction of the TSR; (**c**, **f**) Void fraction of the SRR.

As expected, $\langle C \rangle$ is well captured by all three modelling approaches (Fig. 5**d**), as each model was fitted to the measured data. With respect to the contributions from the TSR and SRR, both the conventional two-layer model and the two-state convolution model reproduce the mean void fraction trends more accurately than the superposition model (Figs. 5**e**,**f**). This reflects the fact that the latter does not explicitly account for the layered flow and is therefore less constrained by the physical structure. Note that $(\langle C \rangle_{\mathrm{TSR}})_{\mathrm{meas}}$ and $(\langle C \rangle_{\mathrm{SRR}})_{\mathrm{meas}}$ were evaluated by integrating the measured void fraction data points over the TSR and SRR regions, respectively.

Overall, models that incorporate the TSR–SRR distinction, either explicitly (conventional two-layer) or probabilistically (two-state convolution), capture the mean void fraction decom-

position more accurately. In contrast, the superposition model, while reproducing the general magnitude, cannot resolve the individual contributions from each region, highlighting the importance of including vertical flow structure in predicting void fraction distributions.

4. Discussion

4.1. Contrasting the three different approaches

The three modelling approaches, conventional two-layer, two-state convolution, and superposition, differ fundamentally in their conceptualization of void fraction distributions. A comparison of their key features, advantages, and limitations is provided in Table 3.

The conventional two-layer model explicitly separates the flow into TSR and SRR, allowing the distinct contributions of each region to be quantified. This approach captures both the magnitude and spatial distribution of void fraction components, and preserves physical realism by linking the void fraction to the local flow structure, which is critical for understanding air bubble transport, air entrainment, and turbulence decay. However, the sharp separation between layers may oversimplify the gradual transitions and intermittent overlap that occur in natural flows.

Table 3. Comparison of the conventional two-layer, two-state, and superposition models.

Aspect	Conventional two-layer model	Two-state convolution model	Superposition model
Physical Basis & Interpretation	Flow divided into TSR and SRR; parameters correspond to measurable layer properties.	Flow alternates between two dominant regimes (e.g., TSR and SRR); parameters describe regime fractions and transition characteristics.	Profile represented as a combination of contributions across the flow column; parameters are less directly tied to distinct flow states.
Underlying Mechanism	Steady-state distribution governed by mean flow and diffusion; profile is discontinuous at the interface.	Transitions between states are modeled via convolution of probability distributions; profile is continuous.	Applies a uniform mechanism across the column; profile is smooth and continuous.
Advantages	Simple and intuitive; allows analytical solutions; effective for quasi-steady flows.	Captures intermittency and layer transitions; parameters have clear physical meaning.	Flexible and smooth; fits complex profiles effectively.
Limitations	Does not represent temporal intermittency or vertical transitions.	Limited to two dominant regimes; introduces additional free parameters	Does not distinguish vertical heterogeneity or layer-specific dynamics.

The two-state convolution model addresses this limitation by introducing a probabilistic occurrence of TSR and SRR structures across the flow depth. This allows partial overlap between the two regions and accounts for spatial variability in air transport. Consequently, the model represents not only the mean void fraction but also the depth-resolved contributions from TSR and SRR more accurately under complex flow conditions. It captures the effects of intermittent entrainment, buoyancy-driven rise, and vortex-induced mixing, providing a more flexible and physically consistent framework for representing vertical air transport than the conventional two-layer approach.

In contrast, the superposition model treats TSR and SRR as fully overlapping over the entire flow depth, computing the mean void fraction as a simple sum of their depth-averaged contributions. While this approach reproduces bulk trends in C and $\langle C \rangle$, it neglects the layered structure of the flow and the associated spatial variations in air transport. Specifically, the model assumes that bubbles generated by different aeration mechanisms are transported according to their original generation, regardless of the local velocity field. In reality, bubbles in the TSR experience local transport with a vertical diffusivity $D^{\#}$, whereas in the SRR, the three-dimensional free-surface produces a higher effective diffusivity D^{*}. This results in two conflicting vertical transport behaviours at the same location, highlighting a conceptual limitation of the superposition approach in capturing the spatial and dynamical complexity of air–water flows.

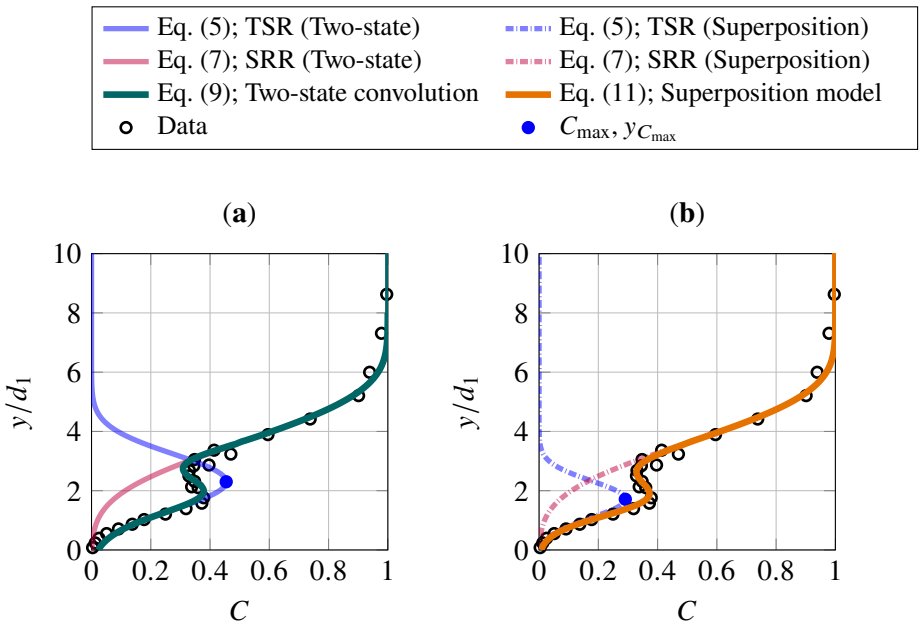

Figure 6. Fitting details for the hydraulic jump with $Fr_1 = 7.9$ at $(x - x_1)/L_j = 0.19$: (**a**) Two-state convolution model (**b**) Superposition model. Equations (5) and (7) are used in both models, but the parameter adjustments differ for each specific model, as indicated here.

For fitting the models to the measured void fraction profiles, we have treated C_{max} and $y_{C_{max}}$ as free parameters (Table 1). While this selection had only a minor impact at locations away from the jump toe, distinct differences were observed near the jump toe, where air entrainment and turbulence are most intense. Figure 6 illustrates the fitted profiles for a hydraulic jump with $Fr_1 = 7.9$, showing that the two-state convolution model assumes that only a portion of the Gaussian TSR profile is captured by the measurements (Fig. 6**a**). As a result, the predicted peak void fraction exceeds the measured values, consistent with a partially masked underlying peak arising from the overlap between the TSR and SRR and unresolved contributions from the turbulent core of the TSR. In contrast, in the superposition model, the observed peak void fraction emerges from the combined TSR and SRR contributions rather than from a maximum of a single component. Consequently, the fitted C_{max} is lower than the measured peak (Fig. 6**b**), indicating that the TSR contribution may be under-represented, even though the total profile matches the measurements.

Overall, the comparison indicates that models accounting for the TSR–SRR distinction provide a more comprehensive and physically consistent representation of void fraction distri-

butions and bubble transport. The superposition model, although computationally simpler and more flexible, may misrepresent the underlying dynamics in flows with pronounced vertical heterogeneity and intermittent aeration. The two-state convolution and superposition models both show improved performance near the jump toe. Furthermore, the superposition model maintains robust fitting toward the end of the roller, where the C_{TSR} profile flattens and $C_{\max}$ and $y_{C_{\max}}$ are difficult to identify, allowing reliable application in the transition from the hydraulic jump to open channel flow.

4.2. Limitations of the present study

The limitations of our study are primarily related to the experimental scope and the range of flow conditions considered, as well as the assumptions underlying the proposed models. Validation is currently restricted to the present dataset, covering a limited range of Froude ($5.1 \leq Fr \leq 7.9$) and Reynolds numbers ($1.32 \times 10^5 \leq Re \leq 18.2 \times 10^5$). It should be noted that the conventional two-layer model has been successfully applied to a much broader range of Reynolds numbers, including prototype-scale flows (Z. Bai et al., 2021; Wang et al., 2023); as a direct extension of this framework, the two-state convolution and superposition models are therefore expected to perform across a similar range. Nonetheless, further research is required to evaluate the generality of these approaches under a wider variety of flow regimes.

5. Conclusion

This study has advanced the modelling of air–water interactions in breaking hydraulic jumps by introducing and validating two novel approaches: the two-state convolution and superposition models. Both methods capture the continuous variation of void fraction across the turbulent shear and surface roller regions, providing a significant improvement over the traditional two-layer framework. Experimental comparisons show that these models accurately reproduce not only the overall void fraction but also the subtle transitions between layers, revealing the complex structure of hydraulic jumps with unprecedented clarity.

Beyond their accuracy, the two models offer complementary strengths: the two-state convolution model provides a physically consistent probabilistic framework, while the superposition model delivers a straightforward and practical tool for engineering applications. Together, they enhance our ability to predict and analyze self-aerated flows, offering robust guidance for the design of hydraulic structures and contributing to a deeper understanding of multiphase flow dynamics. These findings pave the way for more reliable and efficient approaches to managing aerated flows in real-world hydraulic systems.

Acknowledgements

The authors thank Dr Jingmei Zhang and Assoc Prof Ruidi Bai at Sichuan University for assisting with experimental data collection. This research was financially supported by the Science Fund for Creative Research Groups of the Natural Science Foundation of Sichuan Province, China under Grant 2025NSFTD0017, and the National Natural Science Foundation of China under Grant U24B20106. The AI language models ChatGPT (OpenAI) and DeepSeek (DeepSeek) for assistance in revising small portions of the manuscript's grammar is acknowledged. All content, scientific interpretations, and conclusions remain the sole responsibility of the authors.

Data Availability Statement

The data that support the findings of this study are available from the corresponding author upon reasonable request.

Appendix A. Recorded void fraction profiles and model fits

This appendix presents all recorded void-fraction profiles from the experimental campaign for hydraulic jumps with inflow Froude numbers $Fr_1 = 5.1$, 5.9, and 7.9. The corresponding fits obtained using the two-state convolution and superposition models are also shown, enabling a direct comparison between the experimental measurements and the model predictions. Profile numbers correspond to Fig. 3.

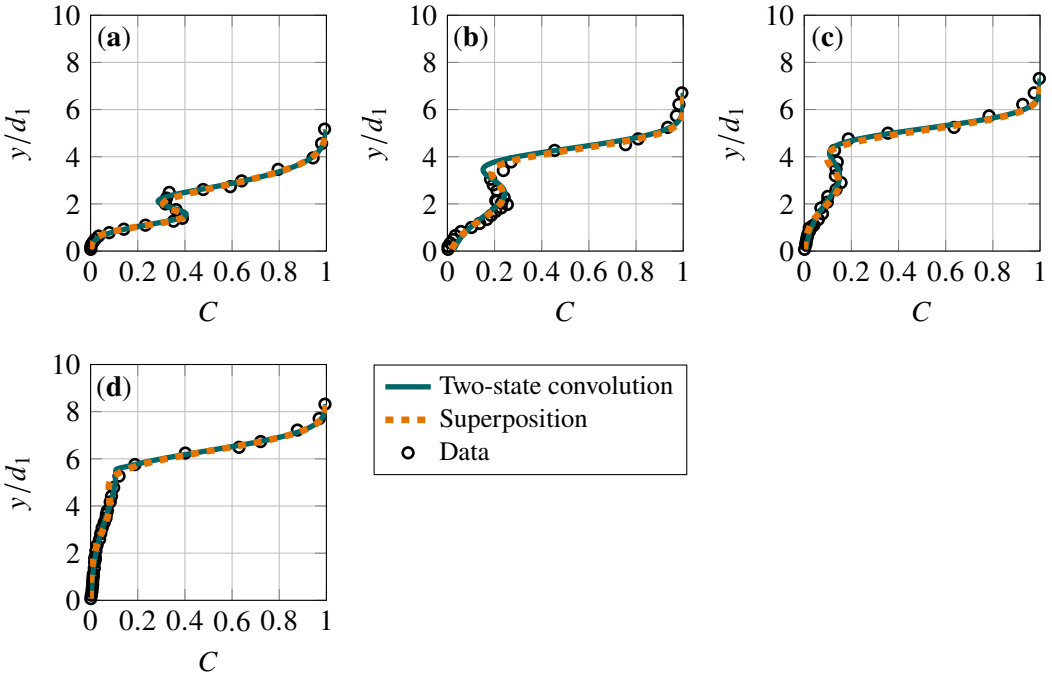

Figure A1. Measured void fraction distributions along the hydraulic jump centerline for $Fr_1 = 5.1$: (**a**) $(x - x_1)/L_j = 0.16$, profile 1; (**b**) $(x - x_1)/L_j = 0.33$, profile 2; (**c**) $(x - x_1)/L_j = 0.49$, profile 3; (**d**) $(x - x_1)/L_j = 0.71$, profile 4.

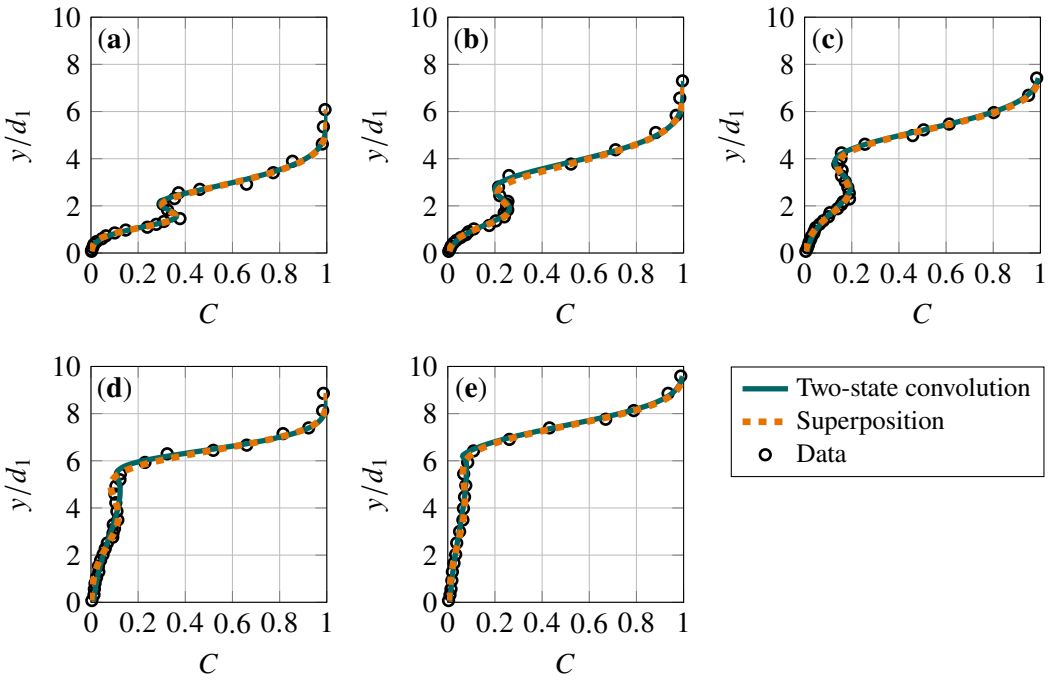

Figure A2. Measured void fraction distributions along the hydraulic jump centerline for $Fr_1 = 5.9$: (**a**) $(x - x_1)/L_j = 0.13$, profile 5; (**b**) $(x - x_1)/L_j = 0.26$, profile 6; (**c**) $(x - x_1)/L_j = 0.39$, profile 7; (**d**) $(x - x_1)/L_j = 0.56$, profile 8; (**e**) $(x - x_1)/L_j = 0.73$, profile 9.

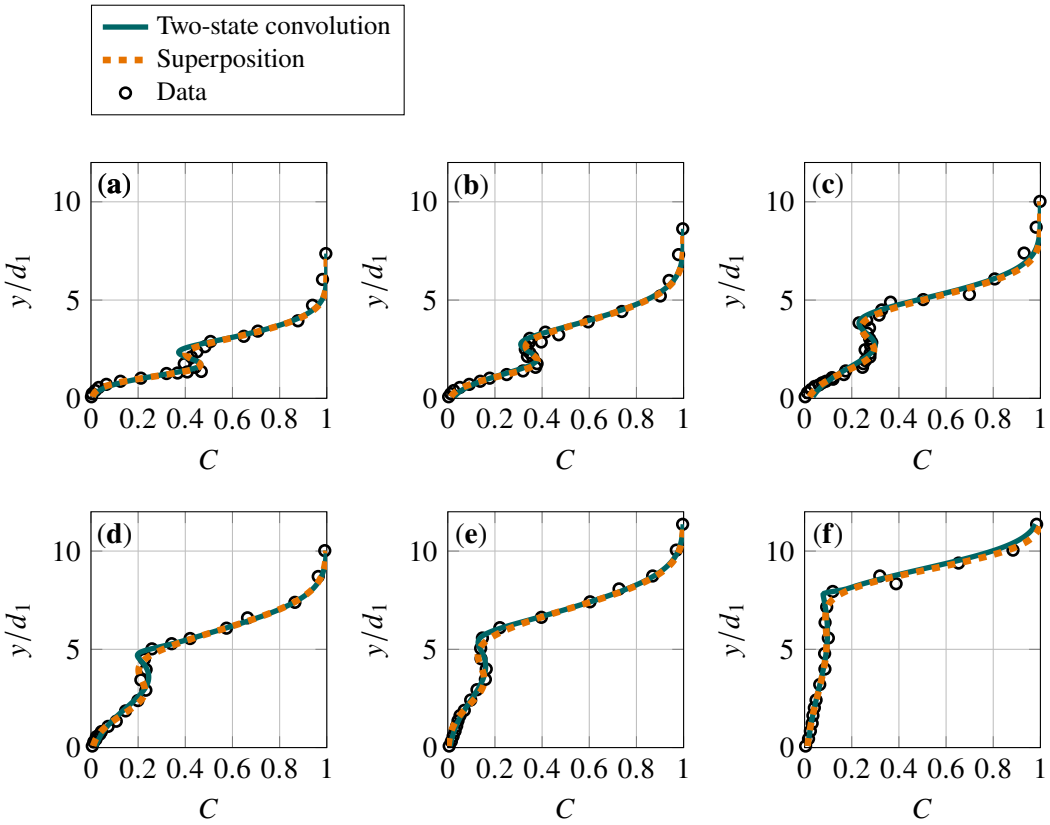

Figure A3. Measured void fraction distributions along the hydraulic jump centerline for $Fr_1 = 7.9$: (**a**) $(x - x_1)/L_j = 0.09$, profile 10; (**b**) $(x - x_1)/L_j = 0.19$, profile 11; (**c**) $(x - x_1)/L_j = 0.28$, profile 12; (**d**) $(x - x_1)/L_j = 0.40$, profile 13; (**e**) $(x - x_1)/L_j = 0.53$, profile 14; (**f**) $(x - x_1)/L_j = 0.68$, profile 15.

Nomenclature

Latin symbols

C	Time-averaged void fraction (-)
$C_{\mathbf{max}}$	Maximum void fraction in the TSR (-)
$C_{\mathbf{SRR}}$	Void fraction in the SRR (-)
$C_{\mathbf{TSR}}$	Void fraction in the TSR (-)
d_1	Inflow depth at jump toe (m)
$D^{\#}$	Dimensionless diffusivity in TSR (-)
D^*	Dimensionless diffusivity in SRR (-)
Fr_1	Inflow Froude number (-)
g	Gravitational acceleration (m/s^2)
L_j	Hydraulic jump length (m)
Q_w	Water flow rate (m^3/s)
q_w	Specific water flow rate (m^2/s)
$Q_{\mathbf{air}}$	Air flow rate at jump toe (m^3/s)
$t_{\mathbf{air}}$	Time probe tip is in air (s)
t_w	Time probe tip is in water (s)
u_r	Bubble rise velocity (m/s)
V_1	Horizontal advection velocity / mean approach velocity (m/s)
X	Transformed longitudinal coordinate in TSR advection-diffusion equation (m)
X'	Dimensionless transformed longitudinal coordinate, X/d_1 (-)
x	Streamwise coordinate (m)
x_1	Longitudinal position of jump toe (m)
y	Vertical coordinate from channel bed (m)
y^*	Mean interface position separating TSR and SRR (m)
y_{50}	Characteristic elevation at which $C = 0.5$ in SRR (m)
y_{90}	Mixture flow depth, defined as vertical position where $C = 0.9$ (m)
$y_{C_{\mathbf{max}}}$	Elevation of maximum void fraction in TSR (m)
Y'	Dimensionless vertical coordinate, y/d_1 (-)

Greek symbols

Γ	Probability of occurrence in two-state convolution model (-)
σ^*	Standard deviation of interface fluctuations in two-state convolution model (m)
Ψ_1	Normalized vertical coordinate in TSR profile (-)
Ψ_2	Normalized vertical coordinate in SRR profile (-)
ν	Kinematic viscosity of water (m^2/s)

Indices and operators

a	Air
w	Water
calc	Calculated
meas	Measured
max	Maximum
SRR	Surface Roller Region
TSR	Turbulent Shear Region

References

Bai, R., Tang, R., Murzyn, F., & Wang, H. (2023). Pre-aerated classic hydraulic jump downstream a partly-stepped chute. *Journal of Hydraulic Research*, *61*(2), 260–271.

Bai, Z., Bai, R., Tang, R., Wang, H., & Liu, S. (2021). Case study of prototype hydraulic jump on slope: Air entrainment and free-surface measurement. *Journal of Hydraulic Engineering*, *147*(9), 05021007.

Brattberg, T., Chanson, H., & Toombes, L. (1998). Experimental investigations of free-surface aeration in the developing flow of two-dimensional water jets. *Journal of Fluids Engineering*, *120*(4), 738–744.

Chanson, H. (1995). Air entrainment in two-dimensional turbulent shear flows with partially developed inflow conditions. *International Journal of Multiphase Flow*, *21*(6), 1107–1121.

Chanson, H. (2002). Air-water flow measurements with intrusive, phase-detection probes: can we improve their interpretation? *Journal of Hydraulic Engineering*, *128*(3), 252–255.

Chanson, H., & Brattberg, T. (2000). Experimental study of the air–water shear flow in a hydraulic jump. *International Journal of Multiphase Flow*, *26*(4), 583-607.

Crank, J. (1956). *The mathematics of diffusion*. Oxford: Oxford University Press.

Crowe, C. T., Sommerfeld, M., & Tsuji, Y. (2011). *Multiphase flows with droplets and particles* (2nd ed.). Boca Raton, FL: CRC Press.

Cummings, P. D., & Chanson, H. (1997). Air entrainment in the developing flow region of plunging jets - part 1: theoretical development. *Journal of Fluids Engineering*, *119*(3), 603–608.

Kramer, M. (2024). Turbulent free-surface in self-aerated flows: superposition of entrapped and entrained air. *Journal of Fluid Mechanics*, *980*, A25.

Kramer, M., & Valero, D. (2020). Turbulence and self-similarity in highly aerated shear flows: The stable hydraulic jump. *International Journal of Multiphase Flow*, *129*, 103316.

Kramer, M., & Valero, D. (2023). Linking turbulent waves and bubble diffusion in self-aerated open-channel flows: Two-state air concentration. *Journal of Fluid Mechanics*, *966*, A37.

Krug, D., Philip, J., & Marusic, I. (2017). Revisiting the law of the wake in wall turbulence. *Journal of Fluid Mechanics*, *811*, 421–435.

Long, D., Rajaratnam, N., Steffler, P. M., & Smy, P. R. (1991). Structure of flow in hydraulic jumps. *Journal of Hydraulic Research*, *29*(2), 207–218.

Murzyn, F., Mouaze, D., & Chaplin, J. (2005). Optical fibre probe measurements of bubbly flow in hydraulic jumps. *International Journal of Multiphase Flow*, *31*(1), 141-154.

Rajaratnam, N. (1962). An experimental study of air entrainment characteristics of the hydraulic jump. *Journal of the Institution of Engineers (India)*, *42*(7), 247–273.

Straub, L., & Anderson, A. G. (1958). Experiments on self-aerated flow in open channels. *Journal of the Hydraulics Division, Transactions of the ASCE*, *84*(7), 1–35.

Valero, D., & Bung, D. B. (2016). Development of the interfacial air layer in the non-aerated region of high-velocity spillway flows. instabilities growth, entrapped air and influence on the self-aeration onset. *International Journal of Multiphase Flow*, *84*, 66-74.

Valero, D., Felder, S., Kramer, M., Wang, H., Carrillo, J. M., Pfister, M., & Bung, D. B. (2024). Air–water flows. *Journal of Hydraulic Research*, *62*(4), 319–339.

Wang, H. (2014). *Turbulence and air entrainment in hydraulic jumps* (PhD thesis). School of Civil Engineering, The University of Queensland, Brisbane, Australia.

Wang, H., Bai, Z., Bai, R., & Liu, S. (2022). Self-aeration of supercritical water flow rushing down artificial vegetated stepped chutes. *Water Resources Research*, *58*(7), e2021WR031719.

Wang, H., & Chanson, H. (2015). Air entrainment and turbulent fluctuations in hydraulic jumps. *Urban Water Journal*, *12*(6), 502–518.

Wang, H., & Chanson, H. (2016). Self-similarity and scale effects in physical modelling of hydraulic jump roller dynamics, air entrainment and turbulent scales. *Environmental Fluid Mechanics*, *16*(6), 1087–1110.

Wang, H., & Chanson, H. (2018). Estimate of void fraction and air entrainment flux in hydraulic jump using froude number. *Canadian Journal of Civil Engineering*, *45*(2), 105-116.

Wang, H., Murzyn, F., & Chanson, H. (2014). Total pressure fluctuations and two-phase flow turbulence

in hydraulic jumps. *Experiments in Fluids*, *55*(11), 1847.
Wang, H., Tang, R., Bai, Z., Liu, S., Sang, W., & Bai, R. (2023). Prototype air–water flow measurements in d-type hydraulic jumps. *Journal of Hydraulic Research*, *61*(1), 145–161.